A Systematic Analysis of Basin Effects on Surface Ground Motion

Peyman Ayoubi, [1] **Kami Mohammadi, Ph.D.,** [1] **Domniki Asimaki, Ph.D.** [1]

Abstract

"Basin effects" refers to trapped and reverberating earthquake waves in soft sedimentary deposits overlying convex depressions of the basement bedrock, which significantly alter frequency content, amplitude, and duration of seismic waves. This has played an important role on shaking duration and intensity in past earthquakes such as the M_w 8.0 1985 Michoácan, Mexico, M_w 6.9 1995 Kobe, Japan, and M_w 7.8 2015 Gorkha, Nepal. Although the phenomenon has been understood and addressed in the literature, it has not been fully incorporated in seismic hazard analysis, and Ground Motion Prediction Equations (GMPE). In this study, we perform an extensive parametric study on the characteristics of surface ground motion associated with basin effects using finite element simulations. We use an elastic medium subjected to vertically propagating SV plane waves and utilize idealized basin shapes to examine the effects of basin geometry and material properties. We specifically study the effects of four dimensionless parameters, the width-to-depth (aspect) ratio, the rock-to-soil material contrast, a dimensionless frequency that quantifies the depth of the basin relative to the dominant incident wavelength, and a dimensionless distance quantifying distance of the basin edges relative to the dominant wavelength. Our results show that basin effects can be reasonably characterized using at least three independent parameters, each of which can significantly alter the resultant ground motion. To demonstrate the application of dimensional analysis applied here, we investigate the response of the Kathmandu Valley during the 2015 M_w 7.8 Gorkha Earthquake in Nepal using an idealized basin geometry and soil properties. Our results show that a simplified model can capture notable characteristics of the ground motion associated with basin effects which suggests that such studies can provide useful insights, relevant to the parameterization of basin effects in GMPEs and design code provisions.

[1]Department of Mechanical and Civil Engineering California Institute of Technology. Correspondence to: Peyman Ayoubi <ayoubi@caltech.edu>.

1. Introduction

The effects of material, layering, and geometry of the shallow crust on surface ground motion is referred to as "site effects". One subcategory of site effects, "basin effects", refers to the influence of bowl-shaped loose sedimentary deposits on the amplitude, frequency and duration of earthquake ground motions, that ultimately affects the structural performance ([12], [24]). These changes have played an important role in many past events including the 1985 M_w 8.0 Michoácan, Mexico, the 1994 M_w 6.7 Northridge, USA, the 1995 M_w 6.9 Kobe, Japan, and the 2015 M_w 7.8 Gorkha, Nepal ([28], [37], [27], [4]).

Studies on basin effects date back half a century and have produced several analytical/semi-analytical and numerical idealized models. The out-of-plane (SH wave) problem was studied first due to its scalar nature, and, therefore, its simplicity. Among others, seminal was the work by Aki & Larner (1970) [2], who devised a method (Aki-Larner method) based on Rayleigh ansatz to calculate the elastic wavefield in a layer over a half-space medium with a periodic irregular interface subjected to harmonic SH wave incidence. The resultant scattered wavefield was presented as a linear combination of plane waves with discrete horizontal wavenumber over a frequency range that was defined by the shear wave velocity and depth of the basin. Results revealed strong lateral interference of waves which were absent in the solution of flat layer approximation (FLA, assuming horizontally stratified media). Limitations of the model to simulate basin-modified seismic wavefields included the Rayleigh ansatz, the small periodic length, and the truncation of wavenumber components.

Parallel to Aki & Larner [2], Boore (1970) [9] studied an irregularly shaped layer over half-space for a transient input motion using the finite difference method (FDM). They validated the method against analytical solutions and showed the capability of it within a certain frequency range. They observed a significant Love wave perturbation in the vicinity of the transition zone where both the amplitude and phase

of the wavefield are affected. Later, Boore et al. (1971) [10] compared results from FDM time-domain simulations to the harmonic frequency-domain solution by Aki and Larner for the case of a layer over half-space and a range of basin configurations. They transformed the FDM solution to the frequency domain and applied an exponential time-domain window to remove boundary effects, and showed that while results were in good agreement for two different basin configurations, the late arrivals of strong reverberations could not be adequately captured by the FLA due to the lateral interference caused by non-planar basin shape.

Shortly after, Trifunac (1971) [43], and Wong & Trifunac (1974) [47] used the wave expansion method to devise a semi-analytical solution for semi-cylindrical and semi-elliptical basins, respectively. In both cases, they considered out of plane harmonic wave incidence and concluded that other than a few cases, the FLA cannot reliably predict the 2D response of basins to seismic wave incidence that is governed by complex 2D wave interference. Moreover, they found that increasing the frequency of incident wave would complicate the wave interference in the basins, a phenomenon that can also occur due to the change in incident angle.

Studies on the more complex SV-P (in-plane) problems became more prevalent the following decade. Among others, Bard & Bouchon (1980) [6] studied the problem of in-plane basin response using a modified Aki-Larner method for cosine basins subjected to P and SV incident motions. They considered two cases of low and high-velocity contrasts, and two basin geometries, a narrow (to investigate the entrapment of waves) and a wide (to investigate the surface wave generation). For wide basins with high-velocity contrast, they observed a clear generation of Rayleigh waves and showed that higher Rayleigh modes were excited by SV incident wave because of the lower value of shear wave velocity. Moreover, they concluded that the general wavefield pattern is similar in both P and SV incidence cases, with the maximum amplification corresponding to the direct wave arrival for P-waves, and the Rayleigh wave generation for S-waves.

Later, Dravinski (1982) [18] examined the scattering of elastic waves by an alluvial valley of elliptical shape subjected to harmonic in-plane (P, SV, and Rayleigh) and out-of-plane (SH) incident motions using the boundary integral (BI) method. Boundary methods are attractive due to the lower dimensionality of the problem, compared to FDM, but they are only efficient for configurations with smooth material transitions (no sharp contrasts). They observed that the effects of incident motion frequency and basin depth were interdependent, and concluded that at the low-frequency regime, the SH incident wavefield is less sensitive to basin depth compared to P and SV waves. In addition, for the case of Rayleigh wave incidence (as would be the case e.g. for a basin located next to a surface topographic), they showed a comparable surface displacement amplification to the case of P and SV waves incidence. Dravinski & Mossessian (1987) [19] later studied single and multiple semi-elliptical dipping layers with weakly anelastic material using the indirect boundary integral equation (IBIE) for harmonic P, SV, and Rayleigh incident waves. They observed that the surface displacement strongly depends on the angle of incidence and the distance from the basin edge for a single layer basin. Adding a second, stiffer layer below strongly affected the surface amplification pattern and magnitude, but adding yet a stiffer third layer below didn't cause any additional significant changes. They concluded that shear wave velocity contrast and basin geometry are the dominant governing parameters in basin amplification.

The M_w 8.1 1985 Michoàcan, Mexico earthquake was a turning point in recognizing the significance of basin effects. Despite the large distance ($\geq$ 350km) from the epicenter, Mexico City experienced disproportionately large amplification and very long shaking duration. A large number of studies were prompted in the wake of the event, and were mostly focused on idealized 2D models of the basin ([7], [13], [28]). The ensemble of studies attributed the observed amplification to basin-edge effects and reverberation of earthquake waves in the sedimentary deposits. The consensus was not as strong for the observed ground motion duration, and some studies attributed it to 3D effects [14] not accounted for in 2D models. It was recently shown that the long duration could be attributed to longer period waves reverberating in the deeper sediments of the basin not previously accounted for [15].

Following the 1985 Mexico City Earthquake, 3D models were brought forth to study basin effects in a more realistic setting by simultaneously solving the in-plane and out-of-plane components ([40], [35]). Examples include the work by Hiroke et al (1990) [26], who used an extended Aki-Larner method to study 3D irregularly layered subsurface structures and observed three dominant 3D effects, namely localization, rapid growth, and strong spatial variability of surface waves. Comparison to 2D simulations confirmed that the true amplitude and duration of surface motion cannot be fully reproduced by idealized 2D models. Pitarka et al (1998) [38] used FDM near-fault ground motion simulations with kinematic source models of the 1995 M_w 6.9 Hyogo-ken Nanbu (Kobe) earthquake, and showed that the constructive interference between source and basin was the main reason for the catastrophic consequences of the event.

In the last twenty years, boundary methods (for example [28]) and FDM (for example [45]) have been increasingly replaced by the more computationally efficient and highly accurate spectral and pseudo-spectral methods ([29], [17],

[25]) for regional-scale simulations of basin effects. Notably among others, Komatitsch and Vilotte [30] and Faccioli et al. [21] were the first to adopt the spectral element method (SEM) from the fluid dynamics community [36]. Their formulation of SEM used the Gauss-Lobatto-Legendre quadrature with Lagrange interpolation instead of lower order interpolation functions used in the FEM, which led to a significant reduction in computational time. Among others, Stupazzini et al (2009) [41] used 3D SEM to study basin effects in the Grenoble valley. In addition to basin amplification, they also considered source effects and sediment pseudo-nonlinear response, and found that the hypocenter location and directivity play an influential role in surface ground motion. Moreover, the radiation mechanism and the relative location of the Grenoble valley to the fault strike played a significant role in the . However, they concluded that the nonlinear response was not as important as the above-mentioned factors in this case study.

In the recent years, focus has shifted to large scale simulation case studies ([46], [20]) and some idealized parametric analyses of basin-specific problems ([35], [23], [22]). The daunting computational cost and input parameters required to capture basin effects using realistic source models, crustal structures and near-surface effects, however, have hindered the integration of these effects in GMPEs and engineering design practice; instead, the engineering community still relies gravely on 1D site response models that are not appropriate to capture basin edge physics, when relevant.

In this paper we take a different approach: we use dimensional analysis to conduct a comprehensive numerical parametric study of 2D idealized basin geometries and material properties. Our goal is to identify and prioritize parameters that govern basin effects, which could in turn help to parameterize basin effects in ground motion models (GMM) and engineering design provisions. After verification of our numerical toolbox, we examine the behavior of semi-elliptical and half-cosine basins by varying the material properties, geometrical configuration, and input motion characteristics. To make the results applicable for general basin configurations, we present them in the dimensionless form. Finally, to test our proposed parameterization, we simulate the response of the Kathmandu Valley, Nepal during the 2015 Gorkha earthquake. Our simplified results compare favorably to long period observations, suggesting that simple basin geometries could potentially be used to investigate and parameterize key ground motion characteristics associated with basin effects.

2. Fundamental Physics of Basin Effects

Basin effects arise from a combination of (a) trapping of seismic waves due to impedance contrast and consecutive reverberations of seismic energy, and (b) focusing effects at the edges of a basin, frequently referred to as *basin-edge effects*. Similarly to 1D site response, soil-to-rock impedance contrast plays an important role in the amount of trapped seismic energy in a basin, and thus in the amplification and elongation of seismic motion.

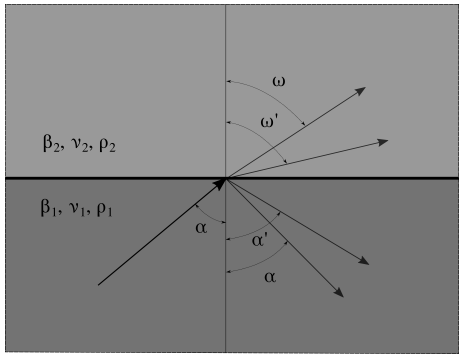

Figure 1. Schematic representation of reflection and transmission of a plane SV wave incident with angle α on a plane boundary of two materials

One can readily quantify the role of material contrast by solving the wave equation for incidence on a two-material interface (Figure 1). By satisfying traction equilibrium and displacement compatibility conditions at the material interface, displacement reflection and transmission coefficients can be computed as outlined in detail by Aki and Richards [3]. To show the variation of the reflection and transmission coefficients as a function of rock-to-soil shear wave velocity contrast, Figure 2 plots the displacement amplification coefficients for the idealized interface problem in Figure 1 subjected to a shear in-plane wave (SV). As can be seen, by increasing the material contrast while keeping all other parameters constant, the amplitude of the reflected S-wave increases and the amplitude of transmitted S-wave decreases. In addition, P-waves are generated at the interface due to mode conversion. Such amplification and mode conversion effects comprise one aspect of basin effects. Basin-edge effects, on the other hand, result from energy focusing and interference of seismic waves in the wedge-shaped edges of a basin. The constructive interference between direct waves and edge-generated surface waves is schematically depicted in Figure 4: when a vertically propagating plane SV wave incites on a sloped subsurface interface between bedrock and sediment, it generates a set of reflected and refracted P and S waves. Focusing on the latter, Figure 4 illustrates the interference of SV direct arrivals, the reflections of SV waves from the bedrock-sediment interface, and the transversely propagating surface waves. This shows a complex interaction of wave components that frequently exacerbates the intensity of the wavefield in a basin.

The combined effects of amplification and basin-edge surface wave generation are illustrated in Figure 3, in the form

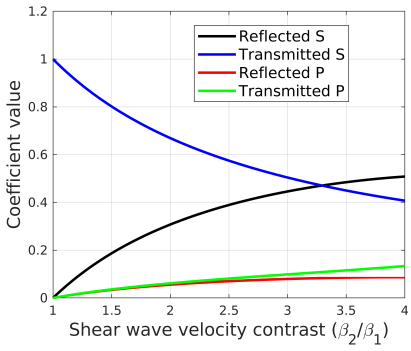

Figure 2. Variation of displacement reflection and transmission coefficients by changing material contrast. This figure shows the case of incident angle $= 5^o$. Different patterns may be observed for higher angles. With reference to Figure 1, medium 1 is softer material

of simulated particle motion on the ground surface of a 20° dipping layer subjected to a unit amplitude vertically propagating SV wave of Ricker type.

Points 1 to 5 lie on the rock outcrop, while points 6 to 16 lie on the surface of the sedimentary dipping layer. Point 6 is located exactly at the tip of the 20° wedge. As can be seen, the basin edge introduces very complex particle motion compared to the frequently assumed horizontally stratified medium which does not generate any vertical component. While its effects are evident on the rock outcrop motion in the vicinity of the wedge tip, it predominantly impacts the particle motion inside the dipping layer. We should also note that while the incident motion was purely horizontally polarized, the ground motion has a significant vertical component arising from mode conversion, as well as very pronounced spatial variability, both of which are likely to affect distributed systems and long components of infrastructure such as pipelines.

3. Description of Numerical Model

The idealized numerical model we used in this study is a 2D basin consisting of two elastic, isotropic, and homogeneous materials for bedrock and basin. We performed analysis of wave propagation in a basin over halfspace using OpenSees, a FEM code that can solve the wave equation in a heterogeneous medium subjected to initial and boundary conditions using an implicit scheme [32]. We discretized the numerical model by requiring 12 quad elements per shortest propagating wavelength to resolve the frequency range of interest based on the dominant frequency of an incoming wave (Figure 5).

Free-field boundary conditions were placed along the side boundaries, at a distance greater than two times the dom-

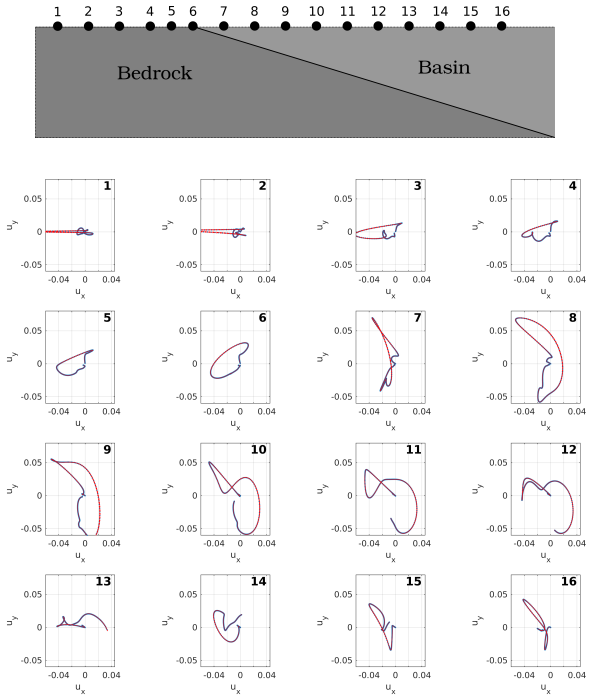

Figure 3. -Particle motion diagram for a set of stations around the basin edge of 20°. Example is shown for material velocity contrast 2, and unit amplitude plane Ricker SV wave with a dominant frequency of 1 Hz.

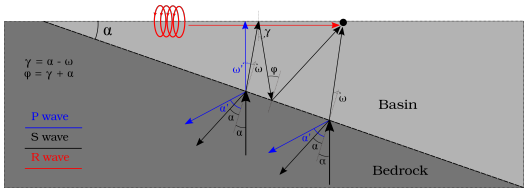

Figure 4. Schematic view of the coupled effect of material contrast and basin edge. P, S and R waves stand for Primary, Shear and Rayleigh waves. β_1 and α_1 are S and P wave velocities in the dipping layer, and β_2 and α_2 are the ones for bedrock. In this figure, $\omega = \arcsin\frac{\beta_1}{\beta_2}\sin\alpha$, $\omega' = \arcsin\frac{\alpha_1}{\beta_2}\sin\alpha$ and $\alpha' = \arcsin\frac{\alpha_2}{\beta_2}\sin\alpha$. Other parameters and angles are shown in the figure.

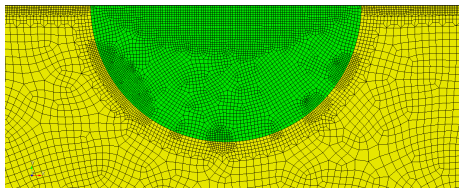

Figure 5. An example of discretized FE domain. The green area shows the basin and the yellow represents the bedrock. The domain is discretized using quad elements.

inant incident wavelength (λ_2, see Figure 10) from basin edges. Free-field (FF) boundary condition comprises S- and P-wave absorbing elements (also known as "Lysmer dashpots" [31]), and free-field equivalent forces corresponding to 1D wave propagation conditions as shown in Figure 7 [16].

The dashpot coefficients for the tangential and perpendicular directions relative to the lateral boundaries, C_s and C_p correspondingly, are estimated as follows:

$$C_s = \rho v_s \tag{1}$$

$$C_p = \rho v_p \tag{2}$$

where ρ is the density of the halfspace, and v_s and v_p are the shear and compressional wave velocities of the halfspace, respectively. Successively, the FF effective forces that represent the stress-field for 1D wave propagation conditions were computed as follows:

$$F_x = -(\rho C_p(V_x^m - v_x^{ff}) - \sigma_{xx}^{ff})\Delta A_y \tag{3}$$

$$F_y = -(\rho C_s(V_y^m - v_y^{ff}) - \sigma_{xy}^{ff})\Delta A_y \tag{4}$$

where F_x and F_y are perpendicular and tangential loads, respectively. V_x^m and V_y^m are nodal velocities in x and y directions computed at each time step during the FE analysis, v_x^{ff} and v_y^{ff} are FF velocities in x and y directions and σ_{xx}^{ff} and σ_{xy}^{ff} are the FF stresses in x and y directions, respectively. The last four quantities are calculated using D'Alembert's method for 1D wave analysis. ΔA_y is the element size in the vertical direction.

For incident motion, we used a unit amplitude vertically propagating plane SV wave of Ricker type [39] (Figure 6, Eq. 5). This is applied as a shear force at the base of the numerical domain where absorbing boundary conditions (Lysmer dashpots) are prescribed. The force is calculated based on Eq. 6 where F_{input} and ΔA_x are input force and element size at the bottom, respectively.

$$Acc(t) = (1 - 2\pi^2 f_0^2 t^2)e^{-\pi^2 f_0^2 t^2} \tag{5}$$

$$F_{input} = \rho C_s \Delta A_x \int Acc(t)dt \tag{6}$$

Synthesizing the above, the vertical side boundaries would ideally respond as 1D columns subjected to vertically propagating shear waves, had there not been a scattered wavefield (albeit weak in this case) that is leaking from the basin sediments at each reverberation. A schematic view of the numerical domain together with prescribed boundary conditions is depicted in Figure 7.

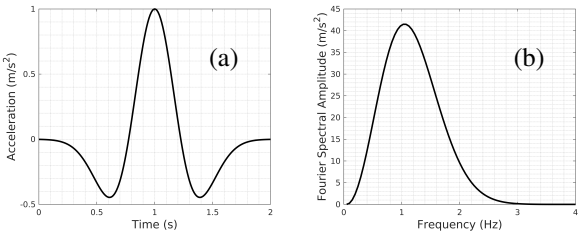

Figure 6. Acceleration input time history, a Ricker wavelet in a) time-domain and b) frequency domain

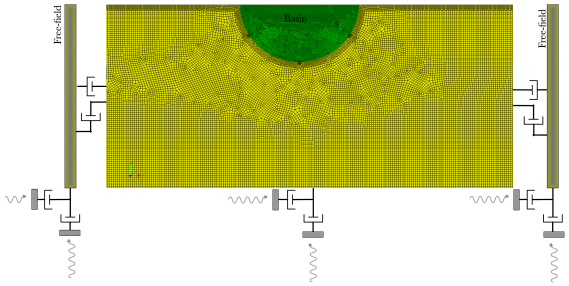

Figure 7. Schematic view of the FEM domain and boundary conditions.

4. Parametric Analysis

In this section, we investigate the variation of surface ground motion with basin geometry, material properties, and input motion characteristics by performing a parametric study on two idealized configurations, Semi-Elliptical (SE) and Half-Cosine (HC). The SE basin is used as a frequently employed idealization that can easily be parameterized. It is suitable to study the physics of wave propagation inside a basin by investigating the effect of dimensionless parameters that will be presented later. The HC basin is used as a more realistic representation of the basin shape while remaining easy to parameterize for geometric and material properties. Eq. 7 gives the mathematical expression of the bedrock-sediment interface depth for an HC basin. Parameters b, D, and a are depicted in Figure 10.

$$\begin{cases} b & |x| \leq D/2 \\ \frac{b}{2}[1 + cos(\frac{\pi(x - D/2)}{a})] & D/2 \leq |x| \leq D/2 + a \\ 0 & |x| \geq D/2 + a \end{cases} \tag{7}$$

The dimensionless parameter space for the problem in hand can be derived using Buckingham's π theorem [11]. For a dynamic problem in elastodynamics, three parameters are needed to define a material. Here, we use v_s (shear wave velocity, denoted β heretofore to avoid parameters with multiple indices), ν (Poisson's ratio) and ρ (density) as representative parameters for each material. In total, we

study the effects of six parameters, namely β_1, ν_1 and ρ_1 of the basin sediments, and β_2, ν_2 and ρ_2 of the bedrock. In addition, a, b and $D + 2a$ are used to define geometry of a basin. Finally, f_0, the dominant frequency of input motion, is used to represent the excitation. Given the ten parameters and three characteristic parameters (length ($[L] = b$), mass ($[M] = \rho_2 b^3$) and time ($[T] = b/\beta_1$)) of the problem, Buckingham's theorem yields 7 dimensionless parameters ($\pi_1 - \pi_7$) defined as follows:

$$\pi_1 = \nu_1,\ \pi_2 = \nu_2,\ \pi_3 = \frac{a}{b},\ \pi_4 = \frac{\beta_2}{\beta_1},\ \pi_5 = \frac{f_0 b}{\beta_1},$$
$$\pi_6 = \frac{\rho_1}{\rho_2},\ \pi_7' = \frac{D+2a}{\lambda_1} = \frac{(D+2a)f_0}{\beta_1} \quad (8)$$

Note that π_7' is derived by multiplying $\pi_7 = (D+2a)/b$ and π_5. In terms of order of magnitude, the dominant dimensionless parameters of our problem are π_3, π_4, π_5 and π_7'. To reduce the computational cost, we perform the parametric study only for these four parameters, and later show that the effects of π_1, π_2 and π_6 are negligible for the problem in hand. Unless otherwise stated, we assume $\pi_1 = 0.33$, $\pi_2 = 0.33$ and $\pi_6 = 1$, as per Kawase & Aki [28].

In the following sections, we first present two verification examples of our numerical model and then examine the contribution of the dimensionless parameters above. For clarity, we refer to π_3 as Aspect Ratio (AR), defined as a over b (see Figure 10); to π_4 as ζ, the dimensionless width of the basin defined as $(D+2a)/\lambda_1$, where λ_1 is the dominant wavelength in the sediments defined as β_1/f_0; and to π_5 as η, the dimensionless frequency. To compare the various realizations of the parametric space, we normalize the peak acceleration amplitude on the ground surface by the peak amplitude on rock outcrop referred to as amplification factor (AF). In addition, we utilize seismogram synthetics (SS) on the ground surface and vector field snapshots to represent the spatiotemporal variation of the wavefield.

4.1. Numerical Model Verification

We present two verification examples of our numerical models: (a) a semi-circular basin from Mossessian & Dravinski (1987) [34], and (b) a trapezoidal basin from Kawase & Aki (1989) [28]. Models are presented using dimensionless parameters explained earlier.

4.1.1. Semi-circular Basin: Mossessian & Dravinski (1987)

The first is a semi-circular basin, with geometry characteristics and material properties described in Mossessian & Dravinski [34] and listed in Table 1. Mossessian & Dravinski used the indirect boundary integral method to compute the steady-state basin response and reported the Amplification Factor (AF) along the surface as the peak ground surface spectral amplitude normalized by the peak incident spectral amplitude (U_x/U_x^{inc}). Figure 8 compares results of the Mossessian & Dravinski to results from this study. To compare our synthetic time-domain results with the steady-state basin response of Mossessian and Dravinski (1987) [34], we extracted the steady-state part of the ground surface displacement, applied the Fast Fourier Transform (FFT), and normalized them by the peak spectral amplitude of the incident motion. The comparison depicted in Figure 8 shows a very satisfactory agreement between the two studies.

Table 1. Material, geometry and incident motion parameters for semi-circular basin study [34]

π_1	π_2	π_3	π_4	π_5	π_6	π_7'
0.333	0.333	1	2	0.5	0.66	1

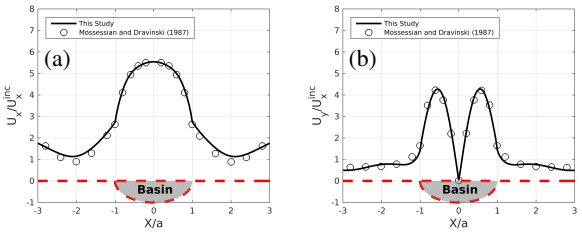

Figure 8. Surface AF in a) horizontal and b) vertical directions for semi-circular basin of Mossessian and Dravinski [34]

4.1.2. Trapezoidal Basin: Kawase & Aki (1989)

The second verification example is the trapezoidal basin response published by Kawase and Aki (1989) [28]. Table 2 shows the parameters we used to simulate this example. Figure 9 shows an excellent agreement of the two studies in the spatiotemporal domain.

Table 2. Material, geometry and incident motion parameters for trapezoidal basin study [28]

π_1	π_2	π_3	π_4	π_5	π_6	π_7'
0.333	0.333	2	2.5	0.25	1	2.5

Results from the two verification tests presented here, where we tested the code against two different geometries and material properties, serve as evidence of the capabilities and accuracy of the numerical model.

4.2. Results

In this section, we present results of the parametric study for each basin geometry, separately. Table 3 lists the dimensionless parameters and the range of values that will be used in the following sections.

First we show results from the SE basin, where we elaborate on the underlying physics of basin effects by first investi-

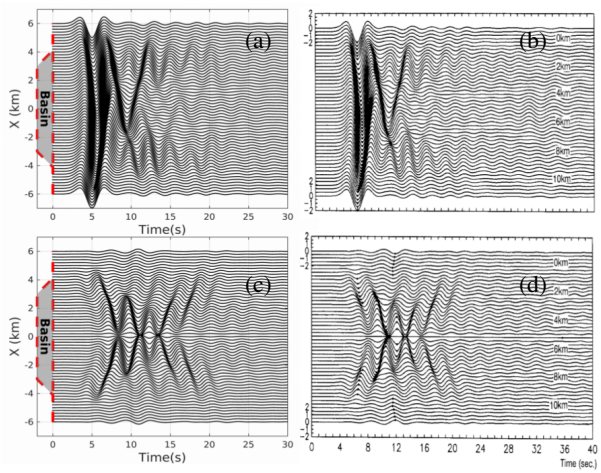

Figure 9. Comparison of ground surface seismogram synthetics in a, b) horizontal and c, d) vertical directions between this study (left) and Kawase & Aki [28] (right). The figures on the right are extracted from Kawase & Aki [28].

Table 3. Parameter space considered in this study

π_3	π_4	π_5	π_7'
0.5, 1, 2, 4	1.5, 2, 3.5, 5	0.125, 0.25, 0.5, 1, 2, 4	0.25, 0.5, 1, 1.5, 2, 2.6, 3.2, 3.8, 4.4, 5, 8, 12

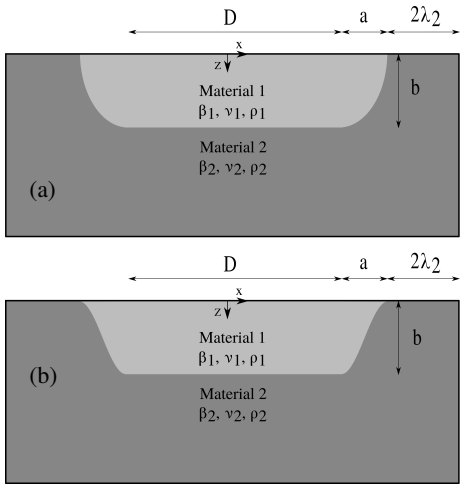

Figure 10. Schematic view of a) SE and b) HC basins. λ_2 is defined as β_2/f_0.

gating the effects of the aspect ratio AR; followed by the effects of dimensionless frequency, η. We also investigate the role of material contrast,β_2/β_1, and dimensionless width of the basin, ζ. Finally, we study the dimensionless parameters that we claimed have a lesser impact on the ground surface motion, namely π_1, π_2 and π_6. For the HC basin shape, a more realistic idealized geometry for studies of basin effects, we next highlight the differences from the SE basin shape, stemming from the shape of basin edges. At the end of the HC section, we also present the effect of material (low-strain) damping on surface amplification. We finally demonstrate the effectiveness of our parameterization by comparing our long-period simplified simulations to the recorded ground motions at the Kathmandu Valley in Nepal during the M7.8 2015 Gorkha earthquake.

4.2.1. Semi-Elliptical Basins

Figure 11 shows the maximum AF of the horizontal component of ground surface motion from the ensemble of SE basin analyses corresponding to $D = 0$, a narrow basin expected to be characterized by a complex 2D wavefield due to the short distance of the two basin edges. The effect of ζ will be discussed later in the article.

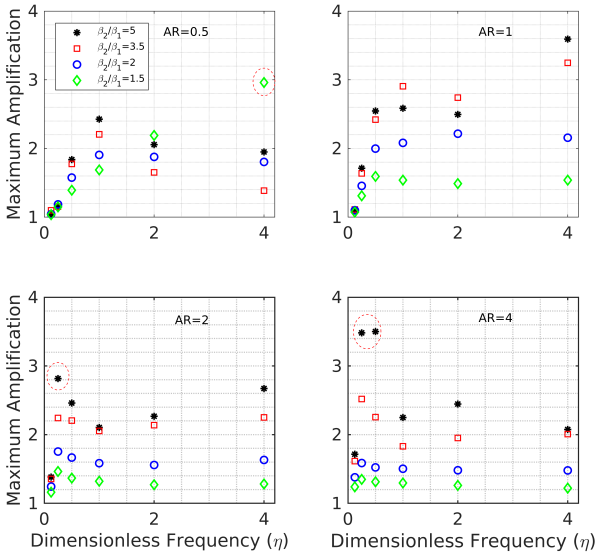

Figure 11. Maximum horizontal AF for all SE analyses. Red circles show unexpected results due to constructive wave interference.

Results show that for a given AR, the amplification factor generally increases with increasing material contrast β_2/β_1. This is not particularly surprising since high β_2/β_1 implies a higher percentage of energy entrapment in sediments, and lower energy leakage. There are, however, a few results that merit further discussion: the case of $AR = 0.5$, $\eta = 4$ and $\beta_2/\beta_1 = 1.5$ (circled in top left subfigure 11) is a deep basin with relatively stiff sediments subjected to high-frequency ground shaking. We observe a very high amplification (AF = 2.95) which is close to the maximum AF that we observed from the ensemble of simulations. As shown in Figure 12, this happens due to the synchronous arrival of direct

waves and edge-induced surface waves at the center of the basin where they constructively interfere. More specifically, Figure 12 illustrates the wavefield evolution in four stages outlined below: (a) The incident wave hits the deepest part of the basin. One can identify the onset of wavefield distortion in the basin. The sediment-rock material contrast plays an important role since it determines the amplitude of the seismic pulse that enters the basin, and regulates the amount of time it takes to reach the basin surface. (b) Vertically incident waves from the base, and laterally propagating surface waves generated at the basin edges travel toward the basin center. (c) Waves interact while waves propagate toward the basin center. (d) Maximum amplification occurs when they constructively interfere at the center.

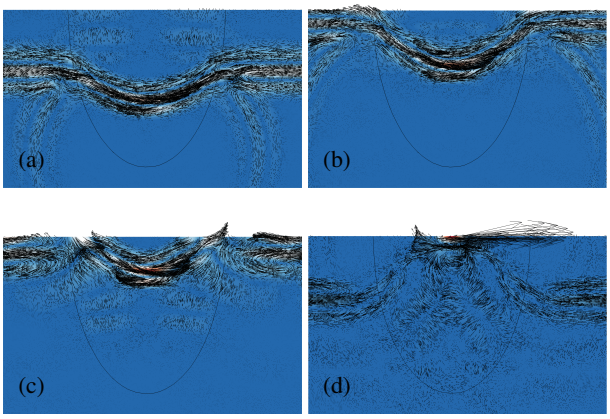

Figure 12. Snapshots of the wavefield for an SE basin with $AR = 0.5$ and $\beta_2/\beta_1 = 1.5$, subjected to vertically propagating shear waves of $\eta = 4$: a) incident wave enters the basin; b,c) body and surface waves travel towards the basin center; d) body and surface waves generate the maximum AF at the basin center.

On the opposite end, for a very shallow basin with very soft sediments, the case of $AR = 4$, $\beta_2/\beta_1 = 5$, and $\eta = 0.25$ to $\eta = 0.5$, a similar phenomenon of constructive interference in the middle of the basin occurs, as shown in Figure 13. On the left, the spatial distribution of amplification is showed where the maximum amplitude occurs in the middle, and on the basis of the seismogram synthetics, takes place at dimensionless time $t^* = 5$. In addition to high AF, due to material velocity contrast, we clearly recognize the reverberations of trapped energy in the sediments, which in addition to large AF, lead to prolonged motion duration.

4.2.1.1. Effect of Aspect Ratio (AR): AR defines the average slope of basin edges, which have shown to dominate the response of most basins during seismic events [27]. In this subsection, we present results of surface amplification for various AR values. The spatial variations of horizontal and vertical amplifications are portrayed in Figures 14 (low frequency incident motion) and 16 (high frequency incident

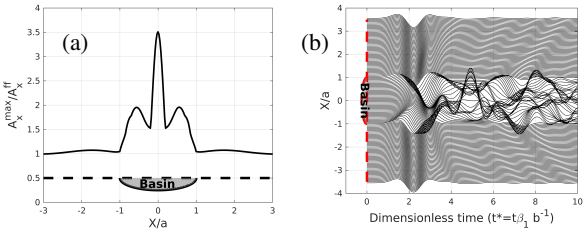

Figure 13. a) AF and b) SS in horizontal direction for $AR = 4$, $\eta = 0.5$ and $\beta_2/\beta_1 = 5$.

motion) for a set of aspect ratios, velocity contrasts, and dimensionless frequencies. Figure 15 illustrates the SS for the top panel of Figure 14, and helps to explain the observed surface amplification.

From these figures, one can observe a large variation associated with varying the AF in both horizontal and vertical directions. Focusing on Figure 14, it is clear that for this particular setting, $AR = 1$ has the largest amplification in the horizontal direction for both material contrasts due to constructive interference of direct arrival of the incident wave and laterally propagating edge-induced surface waves, as can be seen in Figure 14-a and c. For shallower and deeper basins, the wave interference and consequent peak amplification occurs closer to the basin edges. The AF of the vertical component which arises purely from mode conversion (recall that our input motion was a vertically propagating horizontally polarized SV wave) is generated primarily from edge-induced (Figure 15-d,f,h) surface waves except for $AR = 0.5$ (Figure 15-b). For the deepest basin, the basin edges are not playing as important role as their shallower counterparts.

Figure 16 shows how higher frequency input motion would affect the resultant wavefield while other parameters are the same as Figure 14. Increasing the frequency, in general, would result in a more localized interaction of basin and incident motion. This is projected in Figure 16 where higher amplification at basin corners happen over a shorter distance (see Figure 16-a and c). In addition, as a result of more localized interaction, the spatial variation of surface amplification is exacerbated (see Figure 14-b and d) which could cause serious damage to long components of infrastructure system due to torsional particle motion.

Based on the last three figures, the three parameters, namely the coupled behavior of basin geometry, material properties, and frequency content of the incident motion govern the surface ground motion in a basin. For the remainder of the article, we shall use $AR = 1$ as a point of comparison and try to investigate other parameters by keeping the aspect ratio constant.

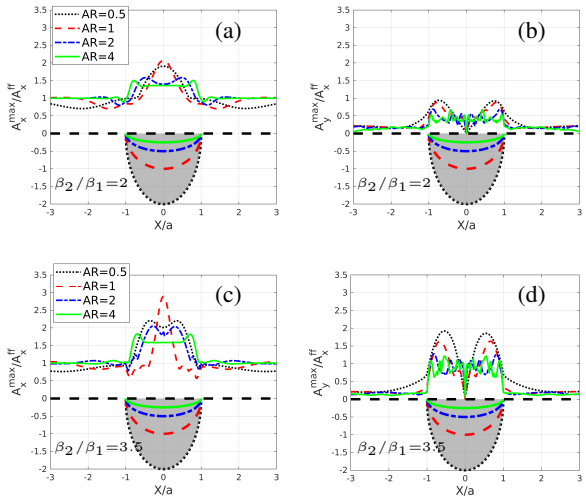

Figure 14. AF in a,c) horizontal and b,d) vertical directions for SE basin for a range of ARs, $\eta = 1$, $\beta_2/\beta_1 = 2$ (top panel) and $\beta_2/\beta_1 = 3.5$ (bottom panel).

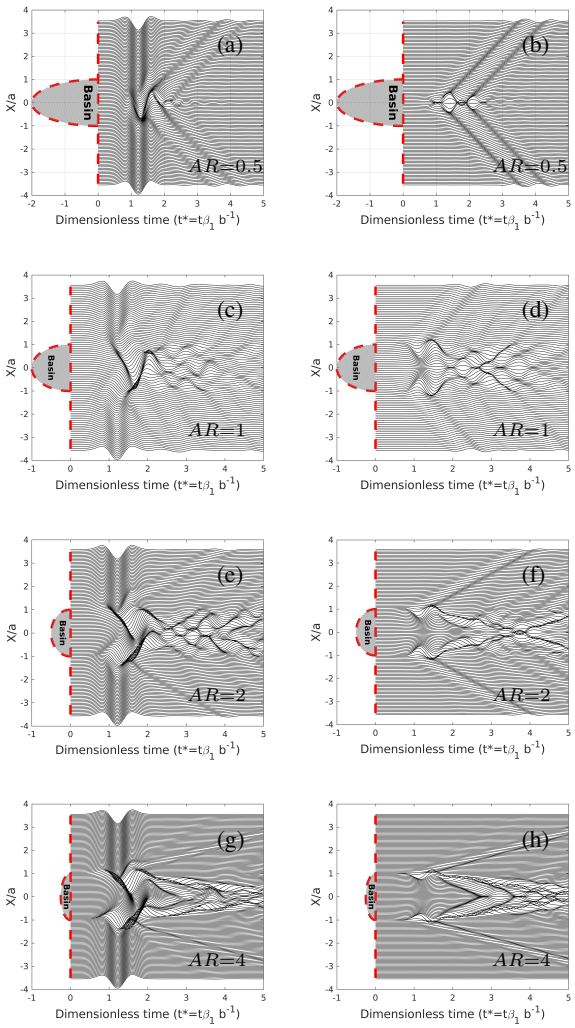

Figure 15. SS for $AR = 0.5$ (top panel), $AR = 1$ (second from top panel), $AR = 2$ (second from bottom panel) and $AR = 4$ (bottom panel) in a, c, e, g) horizontal and b, d, f, h) vertical directions. $\eta = 1$ and $\beta_2/\beta_1 = 2$ are assumed.

4.2.1.2. Effects of Dimensionless Frequency (η) and Material Contrast (β_2/β_1): Figures 17 and 18 show the effects of dimensionless frequency (η) and material contrast (β_2/β_1) on the AF of surface ground motion for a basin with $AR = 1$. Recall that parameter η measures the basin response sensitivity to an incoming wave by quantifying the relative size of the basin to the incoming dominant wavelength. The physical meaning of the parameter is depicted in Figure 17, where, for $\eta \ll 0.5$ and $\eta \gg 4$, the basin is too small or too large compared to the incident wavelength, respectively. In the first case, the wave barely "sees" the basin (basin-bedrock medium behaves as a halfspace), and in the second case, the basin responds similarly to a 1D two-layer column. Therefore, $\eta = 0.125$ (wavelength 8 times larger than basin depth) results in a negligible vertical component since the basin is too small for the seismic wave to experience substantial mode conversion. This figure also illustrates the aforementioned strong spatial variability of surface ground motion for higher frequencies. Moreover, due to the complexity of the wavefield in the basin, no specific η yields a maximum AF across the basin which can be observed in both the horizontal and vertical components and is more pronounced near basin edges. Figure 18 further details the case of $AR = 1$ by showing the effect of material contrast for different η, and thus illustrating the coupled effect of parameters of interest. The AF of the vertical ground motion component reaches surprisingly high value. While the incoming wave is a plane SV-wave, the AF vertical component near the edges is comparable to the horizontal one, and the spatial variability suggests that structures near the edges would experience not only strong transverse and vertical shaking but also rotational motion. In addition, higher frequency incident motions interact on a local scale with the geometry and material properties of the basin, which affect the ground motion characteristics over shorter distances. The opposite is true for longer wavelengths. For the case of $\eta = 0.5$, both horizontal and vertical AFs reveal that the incident motion interacts with the basin as a whole, a fact evidenced in the smooth spatial variation of AF across the basin. By looking through this figure, the localization effect of frequency increment is obvious. For example, by comparing the AF in Figures 18-b and 18-d, one can see that Figure 18-d indicates a more complex amplification distribution due to higher frequency content.

4.2.1.3. Effect of Dimensionless Width (ζ): So far we have investigated three parameters with $D = 0$ to observe

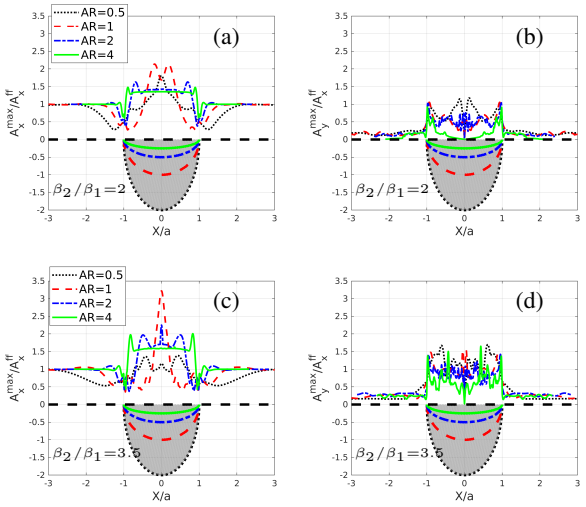

Figure 16. AF in a,c) horizontal and b,d) vertical directions for SE basin for a range of ARs, $\eta = 4$, $\beta_2/\beta_1 = 2$ (top panel) and $\beta_2/\beta_1 = 3.5$ (bottom panel).

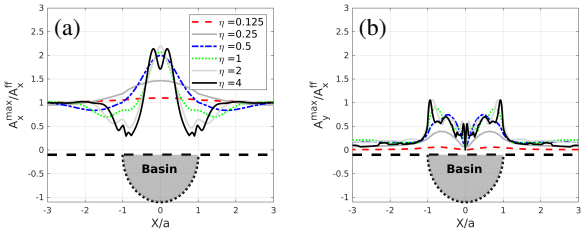

Figure 17. AF in a) horizontal and b) vertical directions for SE-shaped basin with AR=1 and $\beta_2/\beta_1 = 2$

the wavefield in a basin. For this subsection, we focus on edge-induced Rayleigh waves by examining the effects of $D > 0$. Figure 19 shows the effect of the dimensionless width (ζ) on the spatial distribution of surface amplification on a SE basin. Note that the minimum value of ζ corresponds to its value for $D = 0$, namely $\frac{2a}{\lambda_1} = 2\eta AR$. By increasing ζ, the amplification decreases and a separation between two corners appears. This results in a nearly 1D response in the middle of the basin (denoted by a blue star in Figure 19) while the 2D effects dominate as one moves closer to the basin edges. This does not mean that the middle of the basin will experience purely horizontal motion since the Rayleigh wave's traverse motion will still generate significant vertical movement. This phenomenon will be explained in more detail in a later section of this article.

4.2.1.4. Effect of Other Dimensionless Parameters: In this subsection, we examine the effects of three dimensionless parameters we have not investigated yet (see Eq. 8), namely the Poisson's ratio of the sediments (ν_1) and the

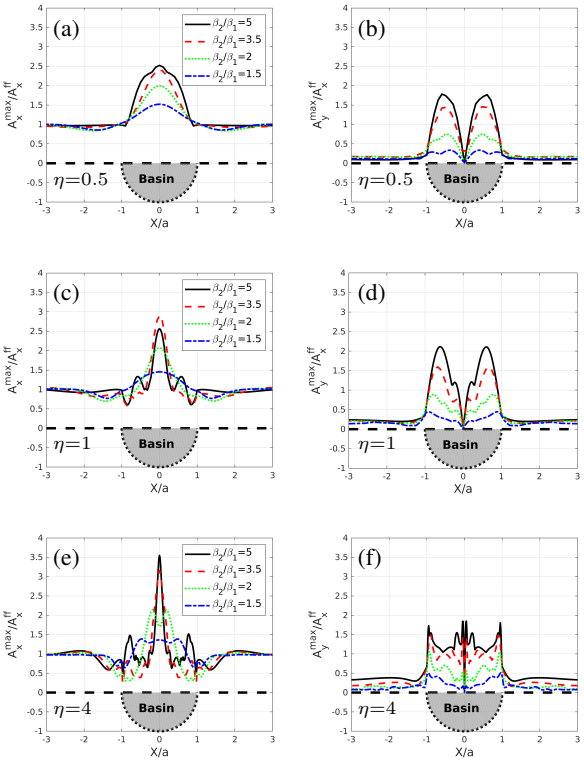

Figure 18. AF in horizontal (left panel) and vertical (right panel) directions for SE basin with AR=1 and a,b) $\eta = 0.5$, c,d) $\eta = 1$, e,f) $\eta = 4$. Three different ηs are shown to also show the coupled effect of material contrast and dimensionless frequency.

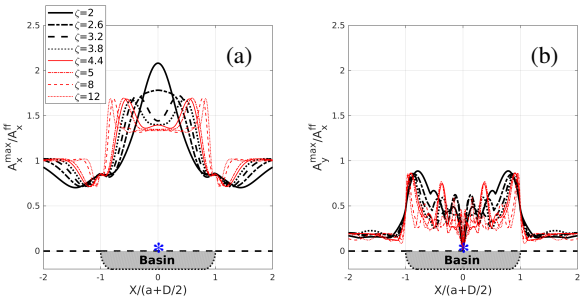

Figure 19. Effect of dimensionless width ($\zeta = (D + 2a)/\lambda_1$) for SE basin for a) horizontal and b) vertical components. $AR = 1$, $\eta = 1$ and $\beta_2/\beta_1 = 2$ are assumed

bedrock (ν_2), and the ratio of mass density of the sediments to the bedrock ($\frac{\rho_1}{\rho_2}$). The range of values we consider is shown in Table 4. Figure 20 shows the effects of Poisson's ratio on the surface amplification for $\beta_2/\beta_1 = 2$ and $\beta_2/\beta_1 = 3.5$, $\eta = 1$ and $AR = 1$. As can be readily seen, the effects of Poisson's ratio are negligible compared to the four main dimensionless parameters we discussed earlier. We should however note here that we expect the effects of Poisson's ratio to be more pronounced for nearly incom-

pressible material behavior ($\nu \approx 0.5$ or undrained loading conditions).

Table 4. Considered parameters for studying effects of π_1, π_2 and π_6

	π_1 (ν_1)	π_1 (ν_2)	π_6 ($\frac{\rho_1}{\rho_2}$)
Value	0.25, 0.35, 0.45	0.2	$\frac{2}{3}$, 0.8

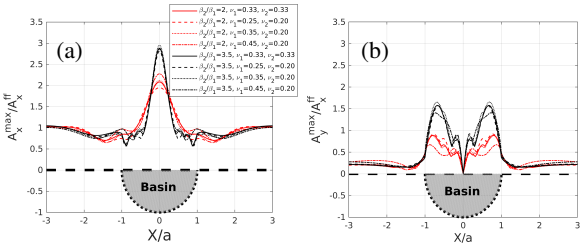

Figure 20. Effect of ν on surface ground motion for two different β_2/β_1 values, for SE basin with $\eta = 1$ and $AR = 1$ in a) horizontal and b) vertical directions

Similarly, Figure 21 shows the effects of density contrast (ρ_2/ρ_1) on the spatial variability of peak amplification, for the case of an SE basin with $\eta = 1$ and $AR = 1$. Results are shown for two velocity contrasts $\beta_2/\beta_1 = 2$ and 3.5. As can be seen, the effects of density contrast are on the order of 5% in the vicinity of the peak horizontal and vertical amplification, which are still considered of secondary importance when compared to the four parameters investigated earlier.

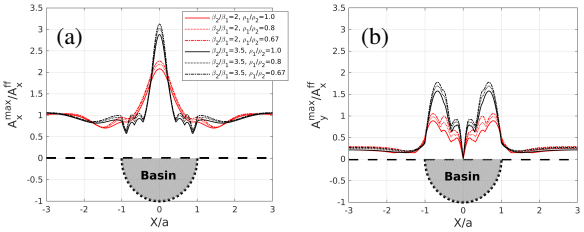

Figure 21. Effect of ρ_1/ρ_2 on surface ground motion for two different β_2/β_1 values, for the case of an SE basin with $\eta = 1$ and $AR = 1$ in a) horizontal and b) vertical directions

4.2.2. Half-Cosine Basins

Although SE models have been widely used as idealized basin geometries ([43], [18]), their sharp corners do not resemble realistic basin edges. In more realistic scenarios, one would expect landscape evolution processes, such as weathering and alluvial or fluvial deposits, to lead to a more gradual transition from rock to sediments near the basin edges. Given the important role of edges in the focusing and diffraction phenomena that govern basin effects (see Figure 22), we here study a more realistic idealized basin shape adopted from the geomorphology literature and referred as Half-Cosine (HC) (see Figure 10 for a schematic representation).

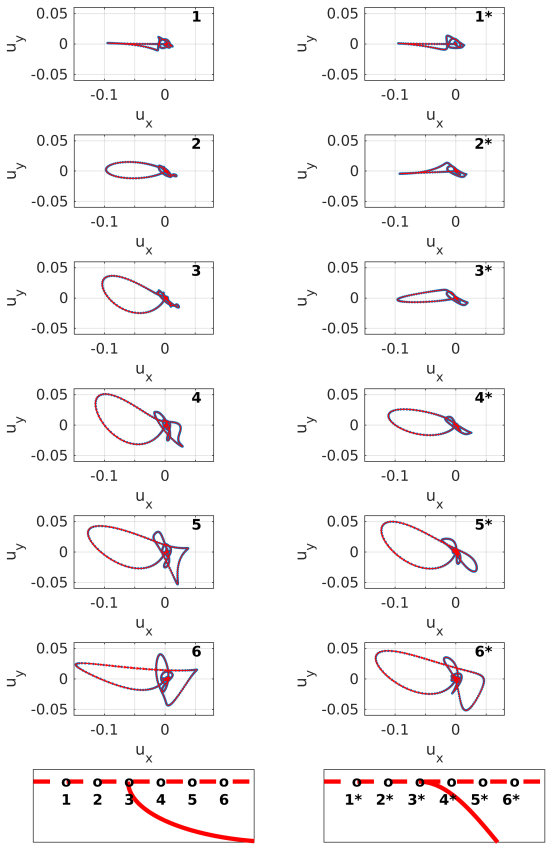

Figure 22. Particle motion comparison for SE and HC basins in the vicinity of basin edge. $AR = 1$, $\eta = 1$ and $\beta_2/\beta_1 = 2$ are assumed.

Figure 22 compares the particle motion of two basin geometries (SE and HC) near the edge with otherwise identical aspect ratios, impedance contrasts, dimensionless width and frequency. The bottom row schematically depicts the geometry of the basin edge and the location where the comparison is taking place. As can be seen, the wavefield is affected by the basin edge geometry (and convexity). The particle motion change would be even more pronounced for higher frequency components. Note that the edge geometry caused a horizontal shift in the wavefield, and it seems that each point on the SE basin corresponds to a further point in HC. For example, points 4 and 4^* have similar particle motions.

For the rest of this section, we focus on the parameters that are directly affected by edge geometry, namely AR and ζ. Although η and β_2/β_1 have been shown to significantly alter the basin's wavefield, their effects do not differ significantly

for a given AR and ζ; results are thus shown for the case of $\eta = 1$ and $\beta_2/\beta_1 = 2$, similarly to SE geometry.

4.2.2.1. Effect of Aspect Ratio (AR): The effects of AR for HC basins are depicted in Figure 23. The effects of edge convexity manifest in the spatial distribution of AF. As can be seen, by changing the basin geometry, the separation of edges does not happen as fast as it happened in the case of the SE basin (Figure 14) because of gradual variation of the basin-bedrock interface depth over distance. This shows how a more realistic basin geometry could affect the amplification variation in a basin, especially for shallower ($AR > 1$) configurations that are more prevalent in urban environments.

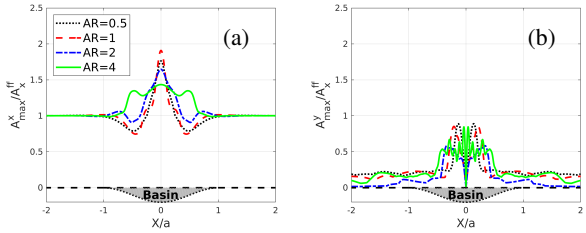

Figure 23. AF for different ARs of HC basins of $D = 0$, $\eta = 1$ and $\beta_2/\beta_1 = 2$ in a) horizontal and b) vertical directions.

4.2.2.2. Effect of Dimensionless Width (ζ): Figure 24 shows the effect of ζ on the surface ground motion in the horizontal and vertical directions. We consider a range of ζ that capture the response of narrow and wide basins. Results illustrate the fading effect of basin edges on the amplification factor close to the basin center. This does not mean that the basin middle would behave as a purely 1D column due to Rayleigh waves traverse propagation within the basin which mostly contributes to the vertical component of surface ground motion. As can be seen, for separation $\zeta \geq 5$, the corner half-cosines have minimal influence in shaping the horizontal amplification, which is evidenced by a uniform spatial distribution of AF over the central part of the basin. Results of the midpoint response for an HC basin are next compared, for representative ζ, to the analytical solution of a 1D two-layered linear elastic soil column [44] subjected to a vertically propagating SV Ricker wave. Figure 25 compares the acceleration time series, Fourier and response spectra at the basin midpoint calculated from 2D wave propagation simulations for $\zeta = 3, 5, 9$, and 12 to the corresponding response of a horizontally stratified 1D layered model. As expected, by increasing ζ, the basin center (denoted by a blue star in Figure 24) increasingly responds like a 1D column as the two basin edges separate. However, even for the case of $\zeta = 12$, edge-induced surface waves traveling horizontally are evident as late arrivals in the midpoint signal, an effect that 1D site response approximations

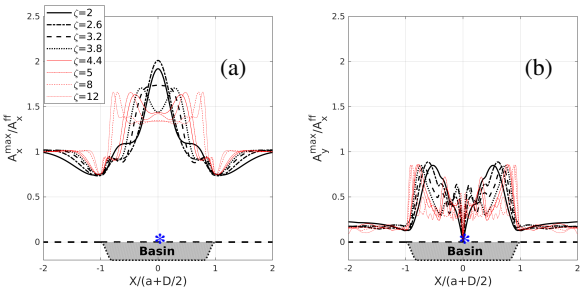

Figure 24. Effect of dimensionless width (ζ) on the surface amplification in a) horizontal and b) vertical directions. $AR = 1$, $\beta_2/\beta_1 = 2$ and $\eta = 1$ are assumed.

.

are not able to capture.

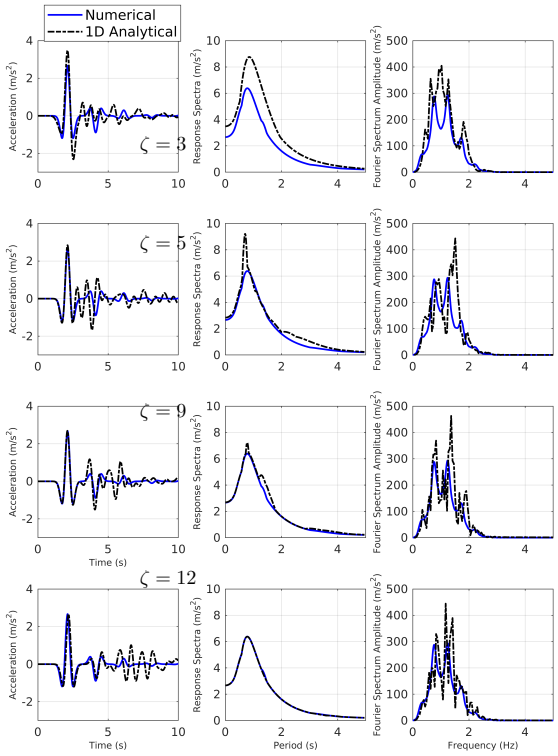

Figure 25. Comparison of the 1D analytical solution with the numerical results at the basin center. The ζ value is shown on the figure. $AR = 1$, $\eta = 1$ and $\beta_2/\beta_1 = 2$ are assumed.

4.2.2.3. Effect of Damping: In reality, during large earthquakes, the soft sedimentary deposit would undergo considerable deformation that causes wavefield attenuation. In this article, we have so far studied the wavefield coupling effects of geometry, material contrast and frequency content without the attenuating contribution of material (low-strain)

damping. Figure 26 shows a comparison between two configurations with $AR = 1$ and $AR = 4$; $\eta = 1$, $\beta_2/\beta_1 = 2$ and a range of realistic damping values. Two damping values $\xi = 2.5\%$ and 5% are considered and the resultant amplification curve is compared with no-damping condition. In order to calibrate Rayleigh damping parameters, $f_{min} = 0.15$ (Hz) and $f_{max} = 3.5$ (Hz) are used while the dominant frequency of input motion is $f_0 = 1$ (Hz) and the fundamental frequency of the soil column corresponding to the deepest part of the basin is $\frac{\beta_1}{4b} = 0.25$ (Hz).

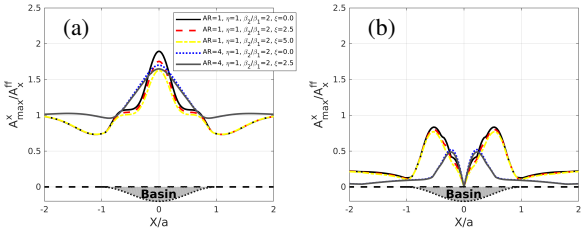

Figure 26. Effect of damping of surface AF in a) horizontal and b) vertical directions. We assumed two different damping parameters ($\xi = 2.5$ and 5.0), $\eta = 1$, and $AR = 1$ and 4.

For the range of geometries and damping values studied here, results are affected by low-strain attenuation in the horizontal direction only at the midpoint of the basin (and no more than $AF \leq 20\%$, and are practically unaffected in the vertical direction). We should, however, highlight that results are shown only for $\eta = 1$, and that higher frequency ground motions are expected to be more strongly affected by low-strain damping effects.

Finally, wavefield snapshots for an HC basin with $AR = 1$, $\beta_2/\beta_1 = 2$ and $\zeta = 3$ are shown in Figure 27. The middle rectangle-like part of the basin behaves similar to a 1D column before the edge generated surface waves arrive, while the corner half-cosines where surface waves originate from amplify the wavefield via focusing. Although the surface wave characteristics differ from the case of the SE-basin due to differences in edge geometry, the same general four-stage wavefield evolution can be observed here as well: (a) body wave arrival, followed by (b-c) surface wave generation at the edges, followed by (d) interaction of body and surface waves in the middle, followed by (e-f) horizontal and vertical wave reverberations in the basin and energy leakage towards the halfspace. The characteristic rotational wave pattern at the base of the basin shown in Figure 27-f is referred to as the "breathing zone" [33], a region where energy transfer occurs between the scattered P- and S-wavefields. HC basins with large ζ are an appropriate representation of wide shallow basin geometries, similar to the trapezoidal geometry used by Kawase & Aki (1989) [28] to study basin effects in Mexico City. In the following section, we use an HC idealized geometry to study basin effects in Kathmandu,

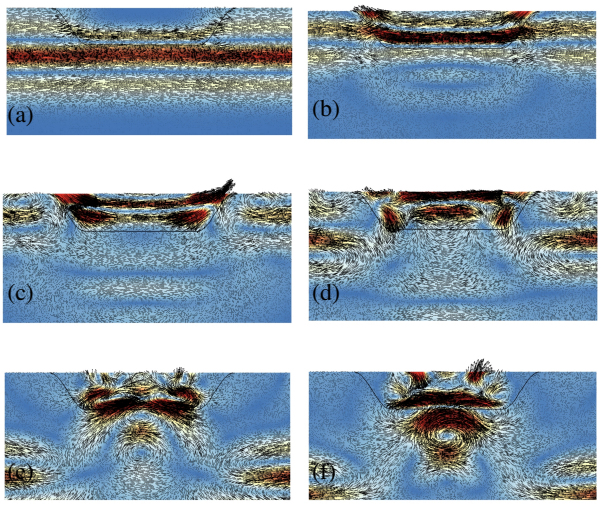

Figure 27. Snapshots of total wavefield for HC basin with AR=1, $\zeta = 5$, $\eta = 1$, and $\beta_2/\beta_1 = 2$. The trapezoidal black line shows the basin boundary.

Nepal, that were observed during the 2015 M_w 7.8 Gorkha Earthquake.

5. Basin Effects in Kathmandu, Nepal: A simplified model approximation

During the 2015 M_w 7.8 Gorkha earthquake [4], macroseismic observations and recorded evidence strongly showed that basin effects had played an important role on the characteristics of strong motion recordings, and the distribution of damage (or lack thereof). To test the extent to which simplified models can capture complexities of basin effects, we here approximate the Kathmandu basin with a HC idealized model. The model was selected to approximate the geometry of the top 0.5 km of basin sediments and is shown in Figure 29 (see Ayoubi et al [5] for more detail). The cross-section of the basin corresponds to the red line shown in Figure 28. The strong ground motion stations depicted in the same figure were installed by Hokkaido University and Tribhuvan University, and they reported the recorded accelerations during the mainshock [42]. These records will be used to evaluate the accuracy of the idealized model presented in this study.

To estimate the basin response of the idealized model, we use a train of two plane SV Ricker wavelets as shown in Figure 30, to excite a range of resonant modes of the basin. The "Data" (Figure 30-b) is used that shows the incident excitation derived using de-convolution at depth of b (see Figure 29) from the East-West horizontal component of recorded motion at reference station KTP. In Figure 30-b, we show the low frequency (LF) and high frequency

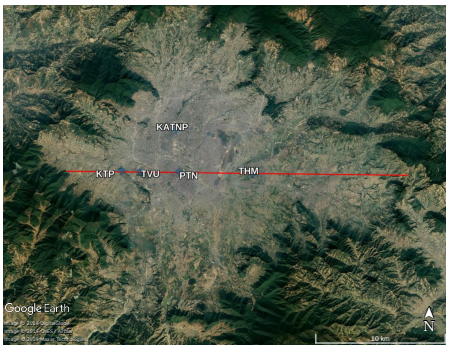

Figure 28. A plan view of Kathmandu basin. The location of strong ground motion stations is shown by their name. The red line shows the cross section that was used by Ayoubi et al (2018) [5] and is used in this study.

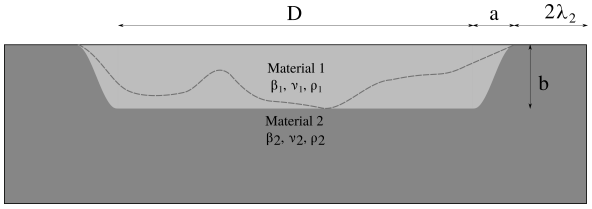

Figure 29. HC basin used in this study. Dashed line shows the realistic geometry of the basin which was used to find the corresponding simplified version in the current study.

(HF) components of input motion which we sum to produce the idealized incident plane wave (Sum Incident Motion in the Figure 30). The time series of each wavelet and the combined input shaking are shown in Figure 30-a. We also assume that the basin is made of an elastic isotropic material with properties listed in Table 5. The bedrock properties were adopted from Wei et al (2018) [46], and the basin shear wave velocity was calculated using 1D velocity profiles published by Bijuckchehn et al (2017) [8] beneath the strong motion stations shown in Figure 28. The profiles are shown in Figure 31, along with the average profile that we used to estimate a 1D approximation of the sedimentary structure inside the basin. The latter was used to calculate the weighted average shear wave velocity for the simplified basin model listed in Table 5.

Table 5. Basin and halfspace parameters with reference to dimensional analysis of section 4.

π_1	π_2	π_3	π_4	π_5	π_6	π_7'
0.333	0.244	3.6	6.4	0.312	0.79	11.15

Figures 32 and 33 show the results of the simplified basin analysis where Figure 32-a and 32-b show the AF of the horizontal, and vertical components on the surface of the basin. Basin edge effects can be readily observed in the

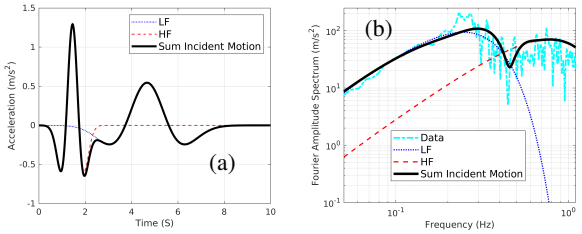

Figure 30. Time series and Fourier spectrum of incident motion from Ayoubi et al (2018) [5] and the current study. The low frequency (LF) and high frequency (HF) show two Ricker wavelets that are summed to derive the input of the numerical simulation (Sum Incident Motion)

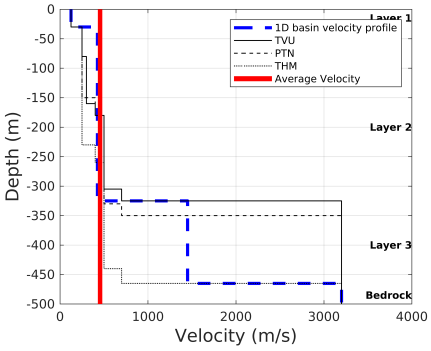

Figure 31. Black lines show the 1D velocity profiles by Bijuckchehn et al (2017) [8]. Blue line shows the averaged and smoothed velocity. We temporally averaged the "1D basin velocity profile" (blue line) to obtain a single value for the shear wave velocity of the basin (red line).

form of localized ground motion amplification and strong spatial variability. The complex spatiotemporal variation of the basin wavefield is depicted by seismogram synthetics in Figures 32-c and 32-d. In this example, the incident motion includes two Ricker wavelets, each triggering the basin response at a different length scale. The constructive interference of the two is leading to the complex AF spatial variation of Figures 32-a and 32-b; although this complexity would be further accentuated in the case of a broadband seismic incident motion, the main features of amplification that include a strong vertical motion in the basin can be adequately captured using this simplified combination of Ricker pulses.

Figure 33 shows a comparison between the amplification factor in the frequency domain for the simplified basin of this study, and the ground motion records from a strong motion array in Kathmandu that recorded the M_w 7.8 Gorkha mainshock [42]. As can be seen, the simplified HC basin model captures some characteristics (low frequency) of the complex ground motion records with acceptable accuracy.

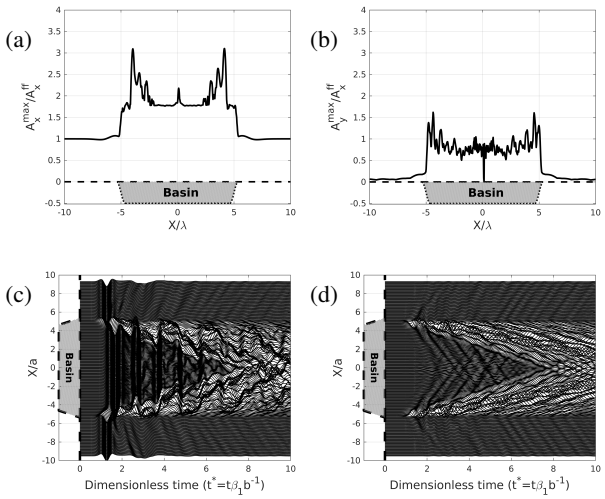

Figure 32. a) Horizontal AF, b) vertical AF, c) Horizontal SS and d) Vertical SS at basin surface

As expected, the simplified model does not capture higher frequencies (more than 1 Hz in this case) since it lacks detailed stratigraphy information that would manifest in high-frequency effects. We should also highlight that the response at station TVU is governed by basin edge effects due to its proximity to the outskirts of the basin; thus, in absence of detailed geometry representation of the basin edge, the predictive capabilities of the idealized model in Figure 33-a are less clear than in the case of Figures 33-b and -c.

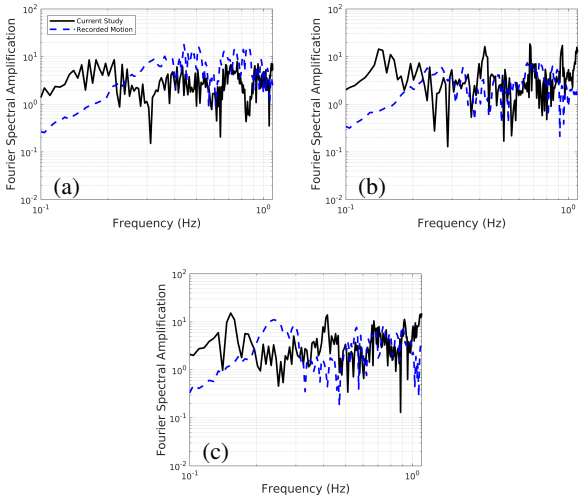

Figure 33. Comparison of simple HC basin ("Current Study"), and recorded motion during the mainshock from Takai et al (2016) [42] for a) TVU station b) PTN station and c) THM station

6. Conclusions

In this article, we performed an extensive parametric study to examine the coupled effects of material properties, interface geometry and ground motion characteristics on the ground surface response of sedimentary basins. We first investigated a simple dipping layer. The calculated surface motion shows that the coupled effect of material contrast and basin-edge can drastically change the wavefield compared to a flat ground with no irregular subsurface, and can produce a substantial vertical motion even when the incident motion is purely horizontal. We then defined two idealized geometries (Semi-Elliptical, SE, and Half-Cosine, HC) and studied their effects for elastic media subjected to vertically propagating SV waves of Ricker type using four dimensionless parameters: aspect ratio (AR), dimensionless frequency (η), material contrast (β_2/β_1), and dimensionless width (ζ).

We first studied AR, a key parameter in describing the geometry of basin edges. We observed that the location and magnitude of maximum horizontal amplification depend on AR; and that for the same AR, SE and HC edge geometries can yield different amplification patterns. The parameter η measures the relative size of a basin to the dominant wavelength. For lower values of η, an incoming wave treats the basin as a whole (very low η motions completely 'miss' the basin), while very high η motions interact only locally with the basin edges. By increasing η, the spatial variation of amplification factor (both horizontal and vertical) enhances, and the AF changes over shorter distances. Our results show that $\eta = 0.125$ had the least impact on the amplification factor, and the response approximated half-space conditions. We next considered material contrast between soil and rock (β_2/β_1), a parameter that controls the energy that enters the basin, and regulates the wave speed in each medium. Increasing material contrast generally resulted in a higher amplification factor due to the entrapment of earthquake waves within the basin, and longer duration. Last, we considered the dimensionless width parameter (ζ), and showed that it can change the pattern of wave interference by separating the whole basin into two 2D problems (corner half-cosine). We observed that for $\zeta \geq 5$, the basin behaves as two decoupled dipping layers with minimal interactions. Finally, we showed that the edge geometry plays a significant role in shaping the surface motion and basin wavefield, and recommended a cosine-shaped basin edge for idealized basin simulations.

Our results show that dimensionless frequency, material velocity contrast, and aspect ratio are the most influential among the seven dimensionless parameters we investigated. The dimensionless width (ζ) was shown to be less influential compared to the above-mentioned three parameters, which is expected since it stands as a proxy for lateral wave reverberations while the scenarios we examined involved

vertically propagating incidence. Other dimensionless parameters such as density contrast, Poisson's ratio or low-strain damping were shown to play a secondary role in this case. This conclusion can be particularly important in developing parameterizations to integrate complex, non-1D phenomena such as basin effects, in data-driven models such as ground motion prediction equations (GMPEs).

In the last section of the article, we approximated the shape of Kathmandu basin, Nepal, with an idealized HC 2D basin, and studied its response compared to the 2015 M_w 7.8 Gorkha earthquake observations obtained on the basin ground surface. We presented the amplification factor computed and recorded on the four strong ground motion stations in the basin and showed that even a simplified model can reproduce key features of the recordings associated with basin effects. We asserted that a more complex model would be required to study the physics of the phenomenon in more detail by incorporating source effects, 2D or 3D basin geometry models, layering and nonlinear site response.

Our findings show that basin effects can be best captured by proxies of three parameters, η, β_2/β_1 and AR. Currently, the most up-to-date GMPEs incorporate basin (really, 1D site) effects through the use of V_{s30} (average shear wave velocity in top 30 meters) and Z_1 (depth to shear wave velocity 1 km/s), while there is evidence that the two parameters can be correlated within the confines of similar geologic units [1]. Our experience shows that parameters η or β_2/β_1 could help improve GMPE parameterization for both 1D and non-1D conditions, while including a basic measure of basin geometry such as AR should be investigated as a means of decreasing aleatoric uncertainty associated with site effects in sedimentary basin settings.

References

[1] N Abrahamson and W Silva. Summary of the Abrahamson & Silva NGA Ground-Motion Relations. *Earthquake Spectra*, 24(1):67–97, 2008.

[2] K Aki and K.L Larner. Surface motion of a layered medium having an irregular interface due to incident plane SH waves. *Journal of Geophysical Research*, 75(5):933, 1970.

[3] K Aki and P.G Richards. Quantitative seismology. 2002.

[4] D Asimaki, Mohammadi K, H.B Mason, R.K Adams, S Rajuare, and D. Khadka. Observations and simulations of basin effects in the Kathmandu valley during the 2015 Gorkha. *Earthquake Spectra*, 33(S1), 2017.

[5] P Ayoubi, D Asimaki, and K Mohammadi. Basin effects in strong ground motion: A case study from the 2015 Gorkha, Nepal earthquake. In *Geotechniccal earthquake engineering and soil dynamics V*, Austin, 2018. ASCE.

[6] P.Y Bard and M Bouchon. The seismic response of sediment-filled valleys-Part II. The case of incident P and SV waves. *Bulletin of Seismological Society of America*, 70(5):1921–1941, 1980.

[7] P.Y Bard, M Campillo, F.J Chávez-Garcia, and F.J Sánchez-Sesma. The Mexico earthquake of Sep 19, 1985- A theoretical investigation of large and small scale amplification effects in the Mexico city valley. *Earthquake Spectra*, 4(3):609–633, 1988.

[8] S.M Bijukchhen, N Takai, M Shigefuji, M Ichiyanagi, T Sasatani, and Y Sugimura. Estimation of 1-D velocity models beneath strong-motion observation sites in the Kathmandu Valley using strong-motion records from moderate-sized earthquakes. *Earth,Planets and Space*, 69(1):97, 2017.

[9] D.M Boore. Love Waves in nonuniform wave guides: Finite Difference calculations. *Journal of Geophysical Research*, 75(8):1512–1527, 1970.

[10] D.M Boore, K.L Larner, and K Aki. Comparison of two independent methods for the solution of wave-scattering problems: Response of a sedimentary basin to vertically incident SH waves. *Journal of Geophysical Research*, 76(2):558–569, 1971.

[11] E Buckingham. On physically similar systems; illustrations of the use of dimensional analysis. *Physical review*, 4(4):345–376, 1914.

[12] H Burton, A Rezaei Rad, Z Yi, D Gutierrez, and K Ojuri. Seismic collapse performance of Los Angeles soft, weak, and open-front wall line woodframe structures retrofitted using different procedures. *Bulletin of Earthquake Engineering*, 17(4):2059–2091, 2019.

[13] M Campillo, P.Y Bard, F Nicollin, and F.J Sánchez-Sesma. The Mexico earthquake of September 19, 1985-The incident wavefield in Mexico City during the great Michoacan earthquake and its intersection with the deep basin. *Earthquake Spectra*, 4(3):591–608, 1988.

[14] F.J Chávez-Garcia and P.Y Bard. Site effects in Mexico-City 8 years after the September 1985 Michoacan earthquakes. *Soil Dynamics and Earthquake Engineering*, 13(4):229–247, 1994.

[15] V.M Cruz-Atienza, J Tago, J.D Sanabria-Gomez, E Chaljub, V Etienne, J Virieux, and L Quintanar. Long duration of ground motion in the paradigmatic valley of Mexico. *Scientific Reports*, 6:38807, 2016.

[16] P Cundall, H Hansteen, S Lacasse, and P Selnes. NEESI soil structure interaction program for dynamic and static problems. *Tech. Rep. 51508-9, Norwegian Geotechnical Institute*, 1980.

[17] G Di-Giulio, R de Nardis, P Boncio, G Milana, G Rosatelli, F Stoppa, and G Lavecchia. Seismic response of a deep continental basin including velocity inversion: the Sulmona intramontane basin (Central Apennines, Italy). *Geophysical Journal International*, 204(1):418–439, 2016.

[18] M Dravinski. Influence of interface depth upon strong ground motion. *Bulletin of the Seismological Society of America*, 72(2):597–614, 1982.

[19] M Dravinski and T.K Mossessian. Scattering of plane harmonic P, SV, and Rayleigh waves by dipping layers of arbitrary shape. *Bulletin of Seismological Society of America*, 77(1):212–235, 1987.

[20] A Esmaeilzadeh and D Motazedian. Sensitivity Analysis for Finite-Difference Seismic Basin Modeling: A Case Study for Kinburn Basin, Ottawa, Canada. *Bulletin of the Seismological Society of America*, 109(6):2305–2324, 2019.

[21] E Faccioli, F Maggio, R Paolucci, and A Quarteroni. 2D and 3D elastic wave propagation by a pseudo-spectral domain decomposition method. *Journal of Seismology*, 1(3):237–251, 1997.

[22] F Gelagoti, R Kourkoulis, I Anastasopoulos, and G Gazetas. Nonlinear dimensional analysis of trapezoidal valleys subjected to vertically propagating SV waves. *Bulletin of the Seismological Society of America*, 102(3):999–1017, 2012.

[23] F Gelagoti, R Kourkoulis, I Anastasopoulos, T Tazoh, and G Gazetas. Seismic wave propagation in a very soft alluvial valley: sensitivity to ground-motion details and soil nonlinearity, and generation of a parasitic vertical component. 100(6):3035–3054, 2010.

[24] SM Haeri and A Fathi. Numerical modeling of rocking of shallow foundations subjected to slow cyclic loading with consideration of soil-structure interaction. *Fifth International Conference on Geotechnique, Construction, Materials and Environment, Osaka, Japan, GEOMATE (CD-ROM)*, 2015.

[25] S Hallier, E Chaljub, M Bouchon, and H Sekiguchi. Revisiting the basin-edge effect at Kobe during the 1995 Hyogo-Ken Nanbu earthquake. *Pure and Applied Geophysics*, 165(9-10):1751–1760, 2008.

[26] M Horike, H Uebayashi, and Y Takeuchi. Seismic response in three-dimensional sedimentary basin due to plane S wave incidence. *Journal of Physics of the Earth*, 38:261–284, 1990.

[27] H Kawase. The cause of the damage belt in Kobe:"The basin-edge effect," constructive interference of the direct S-wave with the basin-induced diffracted/Rayleigh waves. *Seismological Research Letter*, 67(5):25–34, 1996.

[28] H Kawase and K Aki. A study on the response of a soft basin for incident S, P, and Rayleigh waves with special reference to the long duration observed in Mexico City. *Bulletin of the Seismological Society of America*, 79(5):1361–1382, 1989.

[29] D Komatitsch, Q Liu, J Tromp, P Suss, C Stidham, and J.H Shaw. Simulations of ground motion in the Los Angeles basin based upon the Spectral-Element Method. *Bulletin of the Seismological Society of America*, 94(1):187–206, 2004.

[30] D Komatitsch and J.P Vilotte. The Spectral Element Method : An efficient tool to simulate the seismic response of 2D and 3D geological structures. *Bulletin of the Seismological Society of America*, 88(2):368–392, 1998.

[31] J Lysmer and R. L Kuhlemeyer. Finite Dynamic Model for Infinite Media. *Journal of Engineering Mechanics Division*, 95:859–878, 1969.

[32] F McKenna, G Fenves, and M Scott. Open System for Earthquake Engineering Simulation. *Pacific Earthquake Engineering Research Center*, 2000.

[33] T Momoi. Scattering of Rayleigh waves in an elastic quarter space. *Journal of Physics of the Earth*, 28(4):385–413, 1980.

[34] T.K Mossessian and M Dravinski. Application of a hybrid method for scattering of P, SV, and Rayleigh waves by near-surface irregularities. *Bulletin of the Seismological Society of America*, 77(5):1784–1803, 1987.

[35] K.J.P Narayan. 3D basin-shape ratio effects on frequency content and spectral amplitudes of basin-generated surface waves and associated spatial ground motion amplification and differential ground motion. *Journal of Seismology*, 19(1):293–316, 2015.

[36] A.T Patera. A spectral element method for fluid dynamics: laminar flow in a channel expansion. *Journal of computational Physics*, 1984.

[37] A Pitarka and K Irikura. Basin structure effects on long-period strong motions in the San Fernando Valley and the Los Angeles basin from the 1994 Northridge earthquake and an aftershock. *Bulletin of the Seismological Society of America*, 86(1B):S126–S137, 1996.

[38] A Pitarka, K Irikura, T Iwata, and H Sekiguchi. Three-dimensional simulation of the near-fault ground motion for the 1995 Hyogo-ken Nanbu (Kobe), Japan, earthquake. *Bulletin of the Seismological Society of America*, 88(2):428–440, 1998.

[39] N Ricker. The form and nature of seismic waves and the structure of seismograms. *Geophysics*, 5(4):348–366, 1940.

[40] F.J Sánchez-Sesma, L.E Pérez-Rocha, and E Reinoso. Ground motion in Mexico City during the April 25, 1989, Guerrero earthquake. *Tectonophysics*, 218(1):127–140, 1993.

[41] M Stupazzini, R Paolucci, and H Igel. Near-fault earthquake ground-motion simulation in the Grenoble Valley by a high-performance Spectral Element code. *Bulletin of the Seismological Society of America*, 99(1):286–301, 2009.

[42] N Takai, M Shigefuji, S Rajaure, S Bijukchhen, M Ichiyanagi, M.R Dhital, and T Sasatani. Strong ground motion in the Kathmandu Valley during the 2015 Gorkha, Nepal, earthquake. *Earth, Planets and Space*, 68(1):10, 2016.

[43] M.D Trifunac. Surface motion of a semi-cylindrical alluvial valley for incident plane SH waves. *Bulletin of the Seismological Society of America*, 61(6):1755–1770, 1971.

[44] N.C Tsai and G.W Housner. Calculation of surface motions of a layered half-space. *Bulletin of the Seismological Society of America*, 60(5):1625–1651, 1970.

[45] D.J Wald and R.W Graves. The seismic response of the Los Angeles basin, California. *Bulletin of Seismological Society of America*, 88(2):337–356, 1998.

[46] S Wei, M Chen, X Wang, R.W Graves, E Lindsey, T Wang, , C Karakas, and D Helmberger. The 2015 Gorkha (Nepal) earthquake sequence: I. Source modeling and deterministic 3D ground shaking. *Tectonophysics*, 722:447–461, 2018.

[47] H.L Wong and M.D Trifunac. Surface motion of a semi-elliptical alluvial valley for incident plane SH waves. *Bulletin of the Seismological Society of America*, 64(5):1389–1408, 1974.